applied sciences

MDPI

Article

Effect of Incorporating Waste Limestone Powder into Solid Waste Cemented Paste Backfill Material

Jianhua Hu [1,2], Xiaotian Ding [1,2], Qifan Ren [1,2,*], Zhouquan Luo [1,2] and Quan Jiang [1,2]

[1] School of resources and safety engineering, Central South University, Changsha 410083, China; hujh21@csu.edu.cn (J.H.); 175511036@csu.edu.cn (X.D.); Lzq505@csu.edu.cn (Z.L.); jqmose@csu.edu.cn (Q.J.)

[2] Hunan Key Laboratory of Mineral Resources Exploitation and Hazard Control for Deep Metal Mines, Changsha 410083, China

* Correspondence: qifanren@csu.edu.cn; Tel.: +86-181-7513-4802

Received: 19 April 2019; Accepted: 17 May 2019; Published: 20 May 2019

Featured Application: The specific application of the material is to produce cost-saving backfill and to reduce the solid waste in mines.

Abstract: To effectively reuse waste limestone powder, which is a major solid waste around mines, we replaced limestone powder back into a part of cement in solid waste cemented paste backfill (SWCPB) and studied the parameters of pore structures. To optimize the pore microstructure characteristics of SWCPB in mines, two different components and grade tailings were selected. The samples were characterized by scanning electron microscopy (SEM) and nuclear magnetic resonance (NMR) to examine the pore properties and microstructure of SWCPB. The results showed that (1) at the later curing stage, with the optimization of pore characteristics and microstructure through the limestone powder admixture, the strength of SWCFB was guaranteed at a 20% replacement degree of cement. (2) Porosity, macropore proportion, and the average pore radius all negatively correlated with limestone powder content, which were reduced by 7.15%, 46.35%, and 16.37%, respectively. (3) Limestone powder as a crystal nucleus participated in the hydration reaction and was embedded into the product to enhance the strength.

Keywords: limestone powder; cemented paste backfill; image analysis; pore characteristics

1. Introduction

In order to reduce the cost of cement in concrete and to manufacture special cement for various special purposes, many worldwide scholars [1–5] have conducted extensive work on cement substitute materials and concrete additives. Recently, limestone cement has become a recent subject of research, owing to the promising properties of limestone for cost saving and cementing [6,7]. Siliceous limestone powder waste has cementitious activity as it can be reused to replace a part of the cement, leading to an improvement in the properties of concrete and thereby reducing contamination in soil as well as the air pollution [8,9]. Cemented paste backfill (CPB) is an emerging material, which is similar to concrete, that is increasingly being used in mining industries. Hu et al. [10] assessed stone powder as a replacement of cement in CPB, and they studied strength characteristics and reaction mechanism. The results showed that strength of the backfill was greatly reduced at an early stage, and was slightly reduced in the final stages. The effects of adding waste limestone powder into solid waste CPB material still need to be studied.

As a relatively new mine waste management technology, CPB has been extensively applied in underground mine operations around the world because of its significant environmental, technical, and economic benefits [11–14]. Besides, as the mining industry moves deeper into the ground, the

cost of CPB has increased because of unfavorable conditions such as increased pressure in the stope and high environmental standards [15]. Currently, CPB accounts for about 40% or more cement content, although it has only 3–9 wt % of CPB [16]. Therefore, there is urgent need to find another cheap cementation material to replace part of the cement that can reduce the cost and minimize the environmental problems caused by solid waste.

Effects of pore structure on the strength and various properties of CPB are important to know [17]. In fact, researchers need to focus attention on how the pore structure changes in limestone powder. In general, total porosity (n) and pore size distribution (PSD) are the main parameters that are related to the pore structure and can be quantified by using various approaches [18–20]. Among them, scanning electron microscopy (SEM) combined with image analysis (IA) technology is one of the most common methods, which can be directly obtained from the characteristic parameters of pores. Simultaneously, analysis of nuclear magnetic resonance (NMR) spectra can be proposed for identifying material porosity, pore geometry, connectivity, and to characterize PSD material.

The present study focuses on the performance of solid waste cemented paste backfill (SWCPB) containing limestone powder as an additive (0–20%) to cement and tailings as aggregates in SWCPB. SEM-IA and NMR are used to determine relevant pore structure parameters to assess mechanical and hydraulic behaviors. Furthermore, the feasibility of reusing limestone powder in CPB will be evaluated.

2. Materials and Methods

2.1. Raw Materials

2.1.1. Composition Analysis

Tailing samples used in the present study were obtained from an underground lead–zinc mine located in the south of China. The tailings (tailing A and tailing B) from two different mineral processing areas were selected as the combined SWCPB. The binder used in this study was a complex binder made of limestone powder (0–20%) and ordinary Portland cement (OPC) (80–100%). The OPC produced by Changsha Xinxing Cement Plant with C30 grade strength was selected as the major cementing material. Abandoned limestone powder from the mine quarry was selected to replace part of the cement. The proportion of main elements in raw materials was analyzed by using a X-ray fluorescence (XRF, PANalytical B.V., Almelo, The Netherlands) spectrometer, as shown in Table 1.

Table 1. Main mineral composition of tailings A and B.

Element	Tailing A	Tailing B	Limestone Powder	
	Content/%		Compound	Concentration/%
O	34.70	44.38	CaO	57.60
Fe	23.10	12.66	SiO_2	36.87
S	15.86	8.88	Al_2O_3	1.58
Ca	14.03	9.09	MgO	1.17
Si	4.48	16.24	Fe_2O_3	1.17
Mg	2.12	0.40	SO_3	0.74
Zn	1.23	1.14	K_2O	0.27
Al	1.11	3.06	BaO	0.12
As	0.99	1.48	P_2O_5	0.085
K	0.50	0.67	Cr_2O_3	0.085
Sn	0.37	0.24	TiO_2	0.082
Pb	0.34	0.52	MnO	0.081
Sb	0.32	0.35	Na_2O	0.039
Mn	0.14	0.41	SrO	0.039

Siliceous limestone was used as raw material for limestone powder. Table 1 shows that SiO_2 accounted for about 36.87% of content, and SiO_2 reacted with $Ca(OH)_2$ to form C–H–S bonds, promoting

the gelation of filling. Formation of C–H–S bonds served as the crucial part of the hydration reaction, which resulted in the limestone powder used in replacing the cement.

2.1.2. Particle Size Analysis

The main factors affecting the strength of CPB were the composition and particle size of raw materials [21]. The effect of limestone powder for SWCPB could be evaluated according to the change of particle size of SWCPB. Particle size distribution data were obtained by sieve analysis. Experimental analyses of laser particle sizing (Malvern Mastersizer 2000, Malvern Instruments Limited, Malvern, UK) were carried out. Figure 1 presents the particle size distribution data of raw materials.

The majority of particle sizes of tailing A were found to be 110 μm, and that of tailing B was 106 μm, as shown in Figure 1. Both tailings A and B lacked a particle size of around 75 μm, and the proportion of particles under 10 μm accounted for less than 30%, which resulted in the filling of insufficient fine particles in the pores between coarse particles. The distributions of particle size after crushing and grinding are shown in the Figure 1. Here, the majority of particle sizes of limestone powder came to 75 μm, which was up to 3.2%, and the particles under 10 μm were assumed for 43%. According to gradation theory, the addition of limestone powder could improve the particle size distribution of SWCPB.

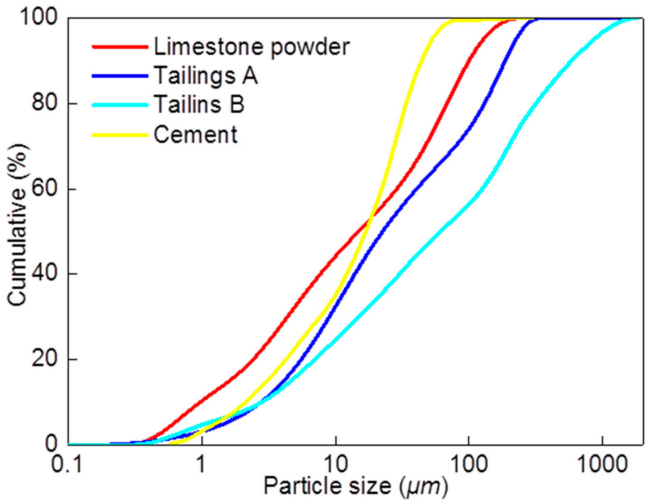

Figure 1. Particle size distribution of raw materials including limestone powder, tailing A, tailings B, and cement.

2.2. Sample Preparation

Considering actual conditions, the ratio of cementitious material to the tailings was 1:4, and the mass concentration was about 70%. In addition, pulping and filling were carried out at room temperature.

According to gradation theory, the ratio of limiting particle size (d60) to the effective particle size (d10) is referred to as the nonuniformity coefficient Cu. By avoiding discontinuous gradation, the grading of backfill aggregate should happen only when $Cu > 10$. Therefore, by introducing the coefficient of curvature, $Cc = (d30 \times d30) / (d60 \times d10)$, and by considering $Cu > 10$ and $1 < Cc < 3$, a different ratio of limestone powder replacement in the cement for the observation group was set. Meanwhile, whole cement (A1 and B1 as control groups) was considered, and the ratio of nonuniform coefficient Cu and curvature coefficient Cc were calculated, as shown in Table 2. However, the Cc values of mixture were below 1.00, which meant its gradation was not ideal in maximizing strength values.

Table 2. Slurry ratio and size parameter of each group. LSP: limestone stone powder; OPC: ordinary Portland cement.

Group	Sample	Mass Content (%)				Cu	Cc
		Water	Tailings	LSP	OPC		
Group A mixture	A1	30	56	0	14	14.56	0.72
	A2	30	56	1.4	12.6	14.68	0.72
	A3	30	56	2.1	11.9	14.80	0.73
	A4	30	56	2.8	11.2	14.93	0.73
Group B mixture	B1	30	56	0	14	40.02	0.71
	B2	30	56	1.4	12.6	44.36	0.64
	B3	30	56	2.1	11.9	44.10	0.64
	B4	30	56	2.8	11.2	43.83	0.65

Three samples of each group (a total of 72 samples) were used as the control to reduce error. The test sample dimensions were 70.7 mm × 70.7 mm × 70.7 mm. Test pieces with dimensions of 15 mm × 15 mm × 15 mm and with the same ratio were designed for NMR analysis. The experiment process is shown in Figure 2.

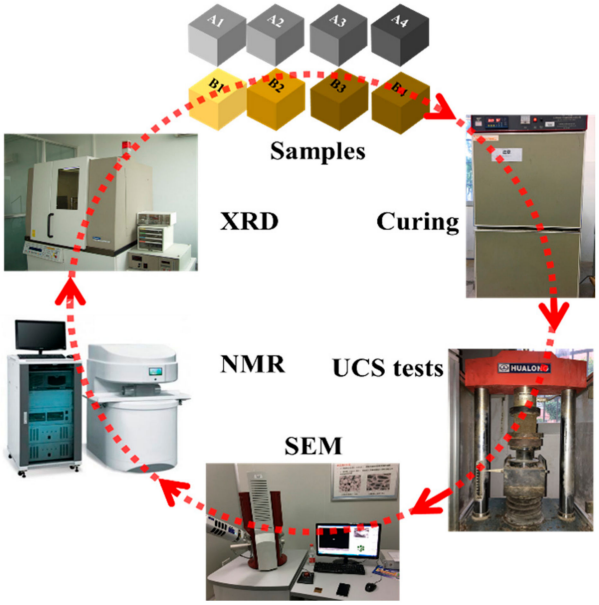

Figure 2. Experimental process with sample preparation, nuclear magnetic resonance (NMR) experiment, uniaxial compressive strength (UCS) tests, and scanning electron microscope (SEM).

2.3. Experimental Methods

2.3.1. Uniaxial Compressive Strength (UCS) Test

Uniaxial compressive strength (UCS) tests were performed on specimens by using WDW-2000 rigid hydraulic pressure servo machine (Ruite, Guilin, China). The displacement rate of loading was 0.5 mm·min^{-1}, and the test standard was GB/T50266-99.

2.3.2. Nuclear Magnetic Resonance (NMR) Analysis

An Ani-MR150 rock magnetic resonance imaging analysis system (Niumag, Shanghai, China) was used to conduct NMR tests on the samples using various mixture ratios and curing times. The average pore distribution of each test piece was calculated to obtain the microstructure distribution parameters of each sample.

2.3.3. Scanning Electron Microscopy-Image Analysis (SEM-IA)

After testing the UCS, a cube sample with a side length of 1 mm was taken from the center of each damaged sample. Then, a metal conductive film on the vacuum coater was applied for SEM tests. SEM images were used to analyze the microscopic pore structure images of each group by using a Czech TESCAN MIRA3 field-emission SEM (TESCAN, a.s., Brno, Czech Republic). Further analysis of SEM images was carried out by using MATLAB (14.0, MathWorks, Natick, MA, USA). With the FRACLAB toolbox in MATLAB, SEM images were analyzed to obtain the grayscale images, binary image, and the fractal dimensions of each sample.

3. Results

3.1. Uniaxial Compressive Strength

The strength of SWCPB directly affected ore body safety and continuity of mining. Figure 3 shows the curve strengths of SWCPB in groups A and B based on UCS test results.

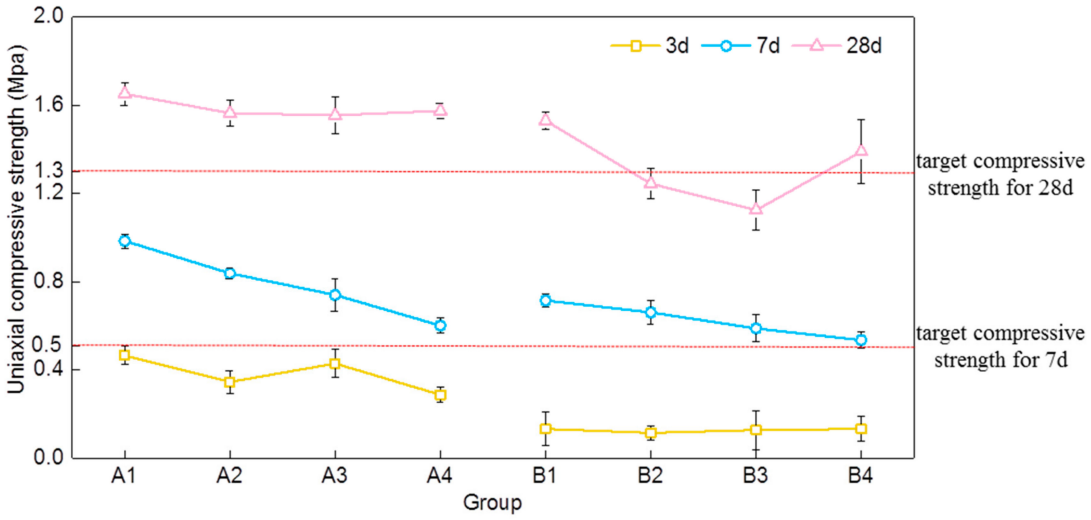

Figure 3. UCS comparison of different mixture ratios of groups A and B.

Results shown in Figure 3 indicated that the strength for three days in group A observed no obvious trend, while with seven days of curing, the strength decreased with the increase of limestone powder replaced. The strengths of A2, A3, and A4 were similar after 28 d. Similarly, for group B, the strength of B4 with 28 d was higher than B2 and B3. Comparing the strengths of group A with B, all strengths of group A were higher than those of group B. It was interesting that there was an apparent retardation in strength development as a result of cement substitution. According to [10], the hydration processes of stone powder cement tailing backfill can be divided into the following four stages: dissolution period, condensation period, infiltration period, and hardening period. At the early curing stage, the groups with cement substitution had less cement to increase the strength, and limestone powders just played a role as a crystal nucleus. However, at the later curing stage, hydration products reacted with SiO_2, which improved hydration reactions and strength.

In addition, according to mining experience, the target strength of seven days is 0.5 MPa, while for 28 days the required strength is 1.3 MPa. As a consequence, the seven-day strength of all groups met the requirements, while the 28 d strengths of B2 and B3 did not meet mining strength requirements of backfill.

3.2. NMR Analysis of Pore Properties

NMR analyses were done using an MiniMR-60 magnetic resonance imaging (MRI) analysis system manufactured by Shanghai Newmai Co. Ltd., China. As the samples were very small, three samples were tested for each group, and their mean values were used for analysis to minimize the error. NMR experiments were carried out for 28 d of curing samples of group A and B, and the pore structure parameters of SWCPB were obtained.

NMR total relaxation (T2) time is related to surface relaxation, loose relaxation of fluid procession, and diffusion relaxation caused by gradient fields [22]. For the water-saturated samples, T2 relaxation time was directly proportional to the pore size and the magnitude of the T2 curve, which directly reflected the porosity of SWCPB samples. Pore size distribution maps were plotted by considering the average amplitude of NMR, as shown in Figures 4 and 5, for groups A and B, respectively.

Three peaks of T2 relaxation time for group A after 28 d of curing can be observed in Figure 4, in which the first peak emerged at about 0.28 ms, the second peak observed at about 11.50 ms, and the third peak appeared at 204.91 ms.

The pore ratio of A1 was shown in Figure 4a, in which the total porosity was about 1.99%. The main pores in A1 were micropores (1st peak accounted for 93.3%), the mesopores accounted for a relatively small proportion (2nd peak accounted for only 1.91%), and there were also many macropores (3rd peak accounted for 4.79%). The pore ratio of A2, as depicted in Figure 4b, showed an increase in total porosity as the limestone powder consisted of fewer active ingredients than the cement. The addition of limestone powder increased the micropores but decreased the macropores, and the change of mesopores was not significant. By further increase of limestone powder to about 15%, as shown in Figure 4c, the total porosity, proportion of micropores, and mesopores were increased, while the amount of macropores was found to be reduced. When the addition of stone powder increased and reached about 20% (Figure 4d), the mesopores remained the same while the micropores increased and the macropores decreased, but the total porosity decreased overall.

The NMR distribution of T2 relaxation time for 28 d of the group B sample showed two peaks in Figure 5, the first peak appeared in the vicinity of 0.30 ms, while the second peak emerged at around 204.90 ms.

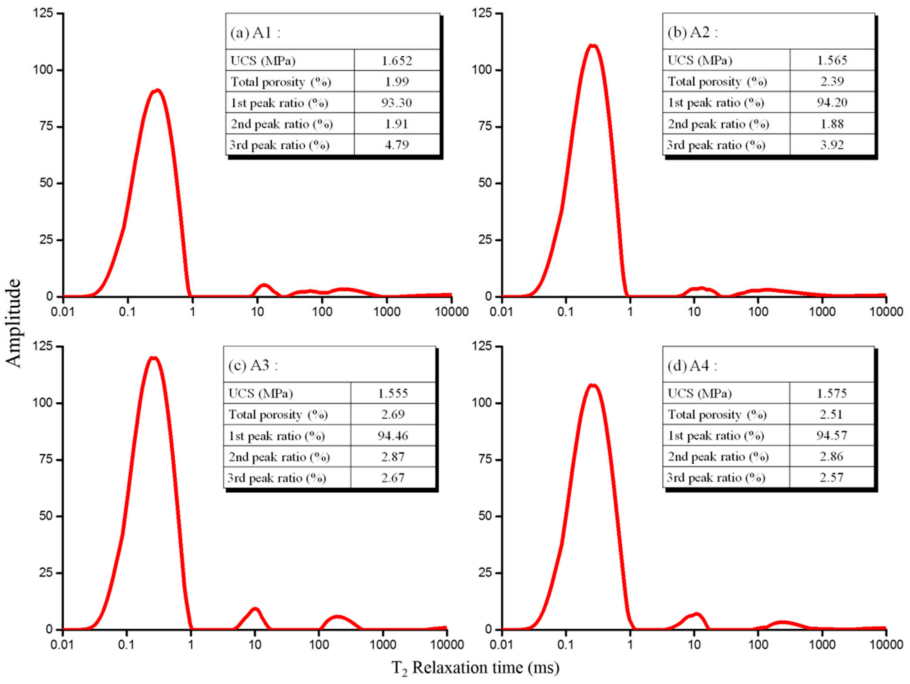

Figure 4. Pore size distribution of group A.

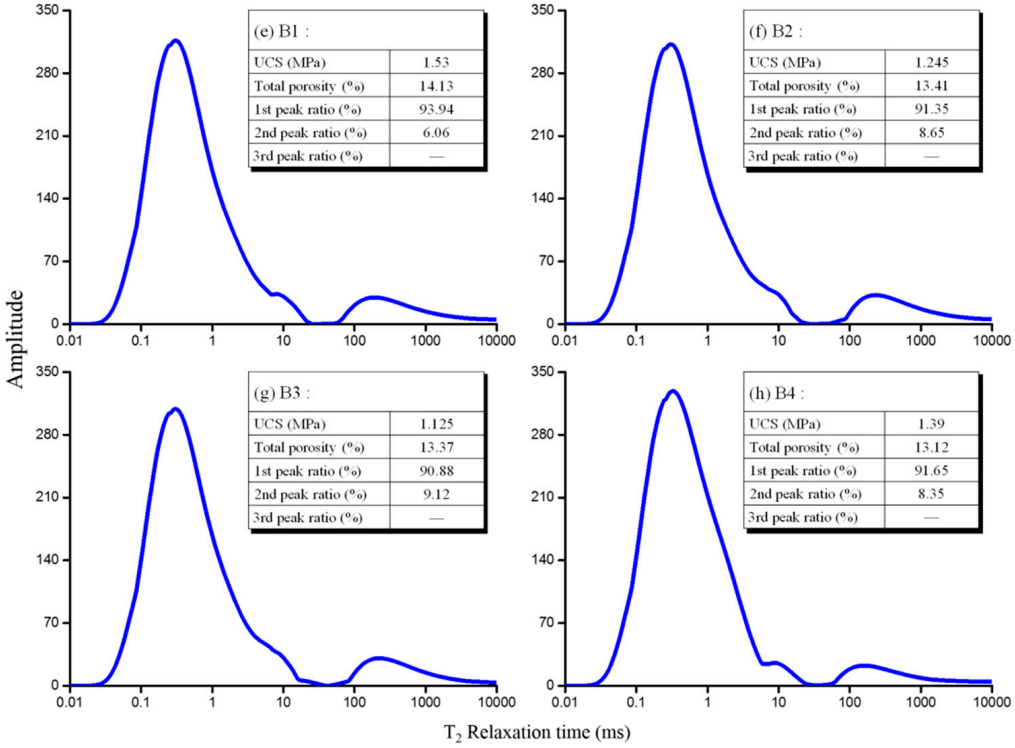

Figure 5. Pore size distribution of group B.

Due to poor grading of group B ($Cu > 40$), there was no obvious difference between the micropores and mesopores. Therefore, the curve had two peaks, and the peak areas of the first peak and the second peak in each group were assumed for 95% or higher of the total area. By increasing the limestone powder, the distribution of micropores decreased, but the macropores increased slightly while the total porosity remained constant. However, when the addition of limestone powder reached 20%, the proportion of micropores increased significantly and the macropores decreased.

3.3. SEM Analysis of the Microstructure

After the initial gelatinization process, the pore structure was formed by the cemented hydration reaction, and it was involved in transferring water, unhydrated material, and storing water. Among the three, the water storage function of the pores maintained the hydration reaction and further enhanced the strength of CPB [22–24]. In this process, the proportion of harmless pores could be increased by reducing the proportion of large pores in SWCPB and simultaneously increasing the proportion of small pores while the total porosity remains intact.

The 28 d curing samples of groups A and B were selected for SEM analysis, at 5000× magnification and a scale size of 10 μm, to study pore distribution, pore morphology, and other characteristics. Figure 6 illustrates SEM images of group A samples for 28 d curing while Figure 7 presents the samples of group B for the same.

The structures of A1, as shown in Figure 6a, were denser, in which the distribution of cementitious materials was uniform, and some of the large particle size tailings were exposed without any connection. Most of the pores were less than 3 μm in diameter. The pore structure of A2 was poorer than A1, shown in Figure 6b. Here, the porosity and pore diameter increased because the limestone powder consisted of fewer active ingredients than cement. When the particles of inert limestone powder were crystallized by the hydration process, the volume was increased, and the body of the crystal was difficult to dissolve as the pores between the tailings were filled. However, the hydration product decreased because of the decrease in cement incorporation; therefore, the microporous structure of A2 was poorer than A1. The pore structures of A3 and A4 were similar to A1, as shown in Figure 6c,d, respectively. Among them, it

was found that the macropores were significantly reduced while mesopores and micropores increased, as compared to Figure 6c,d.

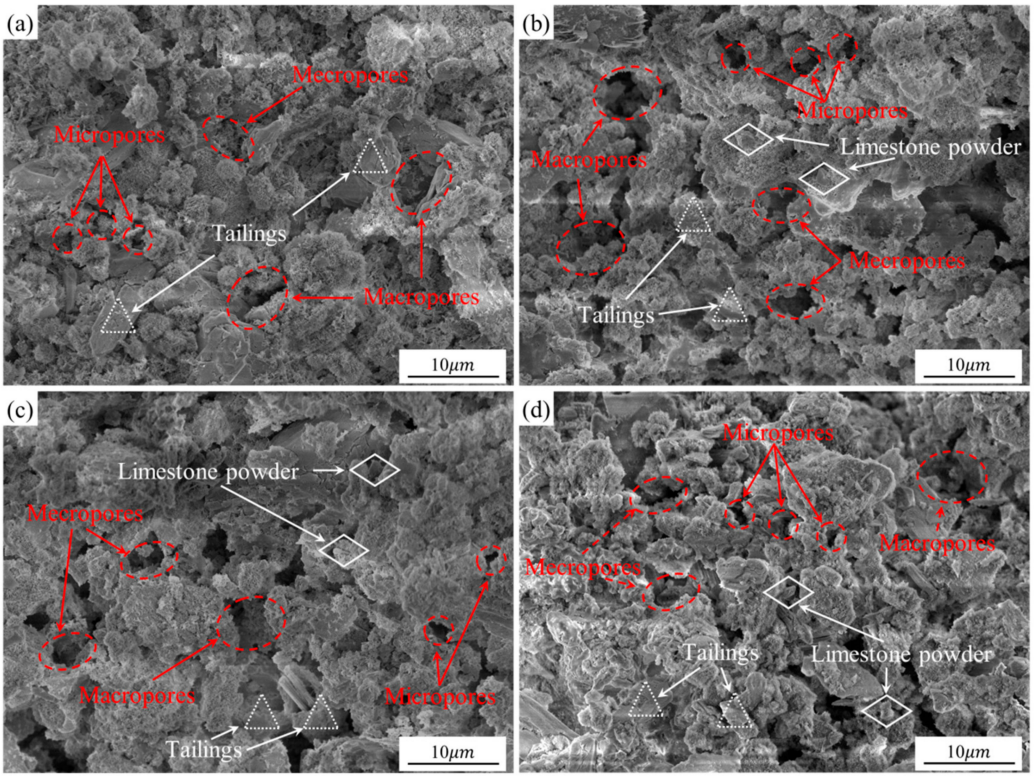

Figure 6. SEM images (5000×) of (**a**) A1, (**b**) A2, (**c**) A3, and (**d**) A4.

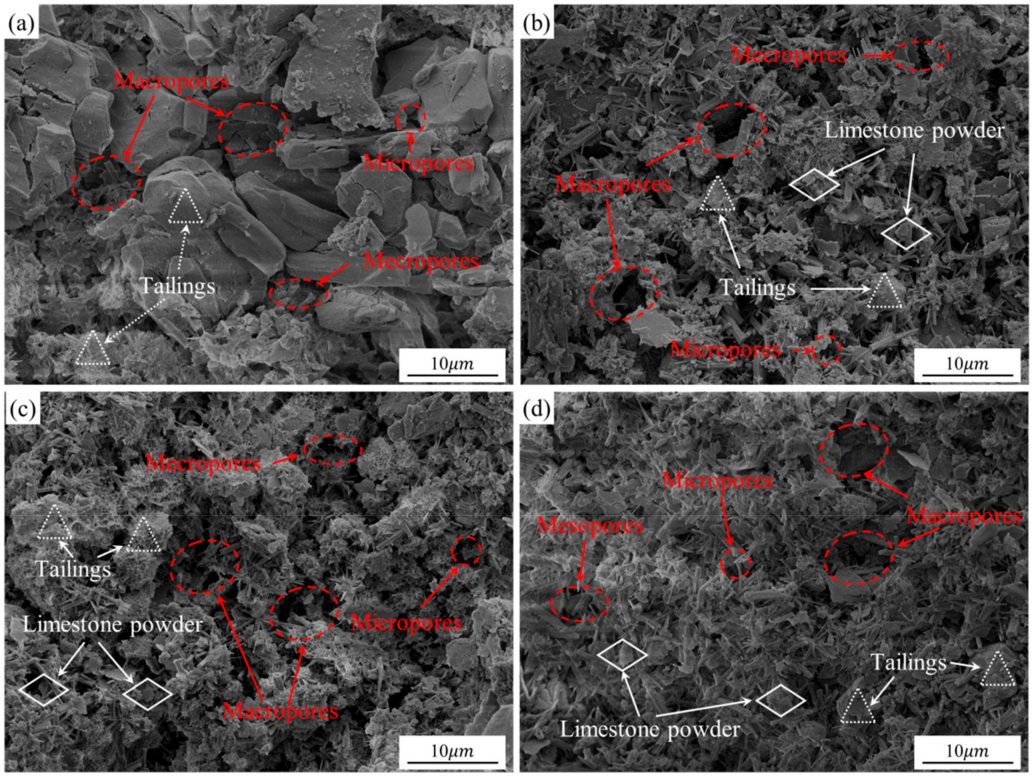

Figure 7. SEM images (5000×) of (**a**) B1, (**b**) B2, (**c**) B3, and (**d**) B4.

The SEM images of 28 d curing age samples of group B showed a small number of large-sized tailings. In the samples of group B, the exposed crystals (mainly Aft) accounted for a large proportion, and the cementitious material (mainly C–H–S gel structures) was not obvious. The structure of group B was looser than that of group A. Without limestone powder particles in backfill, a lot of coarse particles were observed, and there was no particle that filled the gaps between tailings (Figure 7a). The structure of group B4 was denser than that of B2 and B3. Groups B2 and B3 had more macropores, and a lot of macropores combined together to form a complex pore structure, as shown in Figure 7, which meant that the pore structure of B4 was simpler than those of B2 and B3. The calculated NMR porosities of B3 and B4 were almost the same (Table 3); however the average pore radii of B3 were higher than that of B4, which meant that pores of B4 were small, but the distribution was relatively uniform. In addition, group B3 had a large number of pores above 3 μm in diameter, as the number of specific particles that could fill the pores was insufficient. In B4, a large number of fine particles entered into the large pores, and the macropores were divided because there was an increase in the number of particles below 10 μm. Hence, most of the pores of B4 were found to be less than 1 μm in diameter, and the largest pore size reached less than 2 μm in diameter.

Table 3. Binary parameter statistics.

Group	Porosity (%)	Calculated Porosity (%)	Pixel Area	Counting Unit	Calculated Average Pore Radius (μm)
A1	1.99	2.17	16,900	662	1.54
A2	2.39	2.53	19,679	708	1.61
A3	2.69	2.63	20,491	738	1.61
A4	2.51	2.50	19,518	670	1.65
B1	14.13	14.12	110,065	1903	2.32
B2	13.41	12.97	101,102	2209	2.06
B3	13.37	13.97	108,841	1992	2.25
B4	13.12	14.09	109,802	2705	1.94

3.4. SEM Image Quantitative Analysis

SEM images of each group were binarized for quantitative analysis of pore topography data. SEM images (500×) were binarized by using the FRACLAB toolbox in MATLAB. By setting the nearest contrast threshold, NMR porosity was used to generate a binary image together with parallel color inversion. Figure 8 shows two samples that contrasted original SEM images and its binarized images. By implementing count instruction, the pixel count and the unit count of the bright area of binary images were calculated, followed by the calculation of porosity, and then the comparison with NMR porosity, as shown in Table 3. The size of the SEM image was 779,264 pixel units with a total size of 1024 × 761, in which the scale bar was 100 μm length and 185 pixel units. Finally, a single 500× SEM image area was calculated to be 227,710 μm^2.

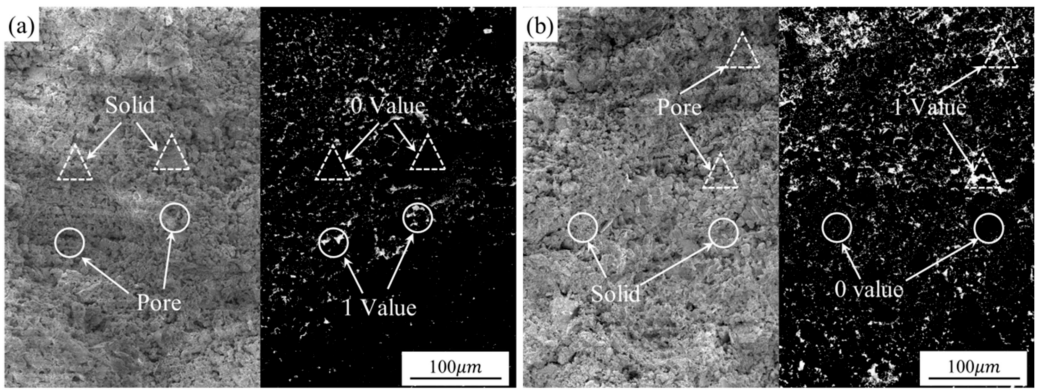

Figure 8. SEM binary image (500×) contrasts of (**a**) A4 and (**b**) B4.

The binarized images had a clearer pore structure than the original images and were easy to measure, as shown in Figure 8. Among them, A4 (Figure 8a) had a uniform pore distribution with most of the pore diameters less than 5 μm and maintaining a compact structure. In a similar way, it was analyzed that B4 had more pores than A4, while for B4 (Figure 8b) a large number of pores had sizes over 10 or even 20 μm.

Table 3 shows that porosity was calculated by using the image processing method of Figure 8. With the help of stereology principles, the calculated porosities of groups A1, A2, B3, and B4 were slightly larger than NMR porosity. The other four cases were reversed. Although there were differences between calculated porosity and NMR porosity, the values were almost the same. The calculated porosity, number of holes (counting units), and the hole radius of group B were significantly greater than in group A. The data shown in Table 3 followed that the average pore radius changed as a result of adding limestone powder. The average pore radius in group A was basically unchanged, but in group B the average pore size first decreased, then increased, but then finally decreased significantly.

4. Discussion

4.1. Pore Characteristics Analysis

For NMR results of group A (Figure 4), porosity deteriorated with the admixture of limestone powder, resulting in an increased value (AVG = 27.14%, max = 35.18%). However, optimization of pore distribution increased the proportion of small holes and decreased the proportion of large holes (AVG = 36.26%, max = 46.35%). Binarization parameters, as listed in Table 3, showed an increase in the number of pores (AVG = 6.55%, max= 11.48%) and thereby slightly increased the average pore radius (AVG = 5.41%, max = 7.14%), which was adverse. The analysis of grading parameters, as listed in Table 2, suggested a nonuniform coefficient A1 value of Cu = 14.56 and a curvature coefficient value of Cc = 0.72 (strive $Cu \geq 10$ and not too large, $1 < Cc < 3$), which increased slightly in the presence of limestone powder admixture in which grading was optimized.

For NMR results of group B (Figure 5), porosity was optimized in the presence of limestone powder with a slight decrease in value (AVG = 5.87%, max = 7.15%), but pore distribution deteriorated as macroporosity increased (AVG = 43.67 %, Max = 50.50%). Binarization parameters, as shown in Table 3, exhibited pore properties that were optimized by increasing the number of pores (AVG = 20.97%, max = 42.14%), and the average pore radius was decreased. The parameters of grading (Table 2) deteriorated after mixing with the limestone powder, in which Cu = 40.02 and Cc = 0.71 for 100% cement group, suggesting a serious loss of intermediate particle size.

The incorporation of limestone powder had a certain influence on the pore properties of SWCFB A and B, and the optimization effect on B group was apparent. The results of NMR depicted in Figure 5 showed that the porosity of 100% cement B1 was 7.1 times of that of A1. When 15% stone powder was mixed with the B group, the porosity could be reduced to 4.97 times of that of group A. In analyzing the binarization parameters from Table 3, the average pore radius ratio of B and A could be reduced to 1.18-fold from the initial 1.51-fold by incorporating 20% stone powder. In group B, the grading (Table 2) did not require any optimization but deteriorated. Hence, the proportion of particles over 100 μm in group B were assumed to be over 40% (Figure 1), which was incompatible with the particle size distribution of limestone powder.

4.2. Microstructure Analysis

From the data presented in Table 1, the existence of SiO_2 was assumed to be about 36.87%, which was involved in the hydration reaction with $Ca(OH)_2$ in the cement. The particles as crystal nuclei were mostly encapsulated in C–H–S gel and embedded in the hydration reaction product as crystalline nuclei. The C–H–S gel with stone powder had higher strength than pure C–H–S gel, but the swelling volume of the hydration reaction decreased compared to the 100% cement group by the same amount of cementitious material.

In the SEM images of group A (Figure 6), the proportion of C–H–S gel was positively correlated with the amount of cement, and the proportion of C–H–S in 100% cement group A1 (Figure 6a) was the largest. In addition, crystals of AFt, a small amount of unreacted $Ca(OH)_2$ crystals, and a certain number of exposed tailing particles were found. The structures of A2, A3, and A4 (Figure 6b–d) were similar. SEM images showed almost invisible AFt, completely reacted $Ca(OH)_2$ particles, and stone powder existed in the form of crystal nuclei. Among the three, A4 had the highest replacement amount of stone powder; its structure was denser and had reduced the porosity, indicating that the microstructure of group A can be optimized with a certain amount of limestone powder.

In group B, the SEM images (Figure 7) revealed a significant increase of AFt than those of group A, approaching towards the formation of C–H–S. $Ca(OH)_2$ almost completely reacted, and a part of the tailing particles was exposed. Limestone powder particles mostly existed among the hydration reaction structures, but some of them were exposed outside. The strength of B4 (Figure 7b) was increased by replacing a certain amount of limestone powder. As a result, the structures of B4 were improved than that of B3 (Figure 7a) with a decrease in large pores, indicating that a certain amount of limestone powder could optimize the microstructure of group B.

4.3. Macro-Strength Characterization

Before and after the incorporation of limestone powder, the UCS of each samples of group B (Figure 3) at each age and mixture ratio were lower than that of the corresponding group A. By analyzing the pore characteristics of A and B, the average porosity (Table 3) of group B was found as 5.64 times, the average proportion of macropores was 2.31 times, and the average pore radius (Table 3) was 1.34 times more than that of group A. The mean nonuniformity (Table 2) was 2.92 times of group A. Parameters obtained from the pore characteristics did not show any beneficial effect. The particle size of C–H–S gel (Figure 6 and 7) increased by the incorporation of limestone powder, but the content of C–H–S gel of group B was significantly lower than that of group A as the microstructural function of limestone powder was not fully demonstrated. In summary, optimization of pore characteristics and microstructure through a limestone powder admixture optimized the strength of SWCFB in group B, but it was to a limited extent. It cannot change disadvantageous aspects of the tailings in group B.

After replacing a part of cement with limestone powder, the strength after 28 d in group A (Figure 3) still maintained a certain level; the strengths of A2, A3, and A4 were found to be in close ranges of 1.565 ± 0.01 MPa; and the proportion of stone powder in the cementitious material could reach 20%. By analyzing the pore characteristics of group A (Figure 4), the porosity and average pore radii of A2, A3, and A4 (Table 3) increased with the replacement of limestone powder, but the proportion of macropores decreased significantly, in which grading (Table 2) was optimized. In contrast, for the microstructure (Figure 6), with an increase in stone powder content, the proportion of C–H–S did not decrease. A2, A3, and A4 were similar in structure. The number of pores in A4 was fewer, and the structure was dense. According to another constant shear test result, the larger the amount of stone powder, the longer it takes for the slurry to reach equilibrium state, whereas the values of equilibrium shear stress and equilibrium viscosity are smaller. That means limestone powder can reduce the dynamic viscosity of slurry and can enhance the slurry-conveying performance. As a consequence, fewer macropores will be formed in backfill after slurries solidify [25]. The strength of samples with cement substitution remained high even after replacing the limestone powder because the proportion of macropores in group A was reduced and the microstructure in the presence of limestone powder admixtures was optimized.

5. Conclusions

To effectively reuse waste limestone powder, portion of cement in SWCPB was replaced by limestone powder. This paper studied the parameters of its pore structures and strength characteristics. The main conclusions are as follows:

(1) The strengths of SWCPB had negative correlations with limestone powder content after three and seven curing days; however, after 28 curing days, limestone powder content did not have a significant impact on strength. Except for groups B2 and B3, the strengths of the other groups can meet mining requirements.

(2) Porosity, macropore proportion, and the average pore radius all negatively correlated with limestone powder content, which were reduced by 7.15%, 46.35%, and 16.37%, respectively. Limestone powder in backfill can reduce the number of pores and the values of average pore radius.

(3) Limestone powder as a crystal nucleus participated in the hydration reaction and was embedded into the product to enhance the strength of SWCPB. Thereby, the pore distribution of backfill was optimized. With optimization of pore characteristics and the microstructure through the limestone powder admixture, the strength of SWCFB can be optimized to a certain extent.

Author Contributions: Conceptualization, J.H. and X.D.; Methodology, Q.R.; Validation, Q.R. and Q.J.; Analysis, X.D. and Q.R.; data curation, Q.R. and Q.J.; Writing—original draft preparation, X.D.; Writing—review and editing, J.H.; Supervision, J.H.; Project administration, J.H. and Z.L.

Funding: The research was supported by (1) The National Key Research and Development Program of China, grant number 2017YFC0602901; (2) The National Natural Science Foundation of China, grant number 41672298.

Acknowledgments: We thank the Gaofeng Mine's management and staff for their valuable support. We thank instructional support specialist Modern Analysis and Testing Central of Central South University. Finally, we thank the two anonymous reviewers for their helpful comments.

Conflicts of Interest: The authors declare no conflict of interest.

References

1. Al-Kheetan, M.J.; Rahman, M.M.; Chamberlain, D.A. Chamberlain. Influence of early water exposure on modified cementitious coating. *Constr. Build. Mater.* **2017**, *141*, 64–71. [CrossRef]
2. Al-Kheetan, M.J.; Rahman, M.M.; Chamberlain, D.A. A novel approach of introducing crystalline protection material and curing agent in fresh concrete for enhancing hydrophobicity. *Constr. Build. Mater.* **2018**, *160*, 644–652. [CrossRef]
3. Kupwade-Patil, K.; Palkovic, S.D.; Bumajdad, A.; Soriano, C.; Buyukozturk, O. Use of silica fume and natural volcanic ash as a replacement to Portland cement: Micro and pore structural investigation using NMR, XRD, FTIR and X-ray microtomography. *Constr. Build. Mater.* **2018**, *58*, 574–590.
4. Celik, K.; Meral, C.; Gursel, A.P.; Mehta, P.K.; Horvath, A.; Monteiro, P.J.M. Mechanical properties, durability, and life-cycle assessment of self-consolidating concrete mixtures made with blended portland cements containing fly ash and limestone powder. *Cem. Concr. Compos.* **2015**, *56*, 59–72. [CrossRef]
5. De Weerdt, K.; Ben Haha, M.; le Saout, G.; Kjellsen, K.O.; Justnes, H.; Lothenbach, B. Hydration mechanisms of ternary Portland cements containing limestone powder and fly ash. *Cem. Concr. Res.* **2011**, *41*, 279–291. [CrossRef]
6. Wang, D.; Shi, C.; Farzadnia, N.; Shi, Z.G.; Jia, H.F.; Ou, Z.H. A review on use of limestone powder in cement-based materials: Mechanism, hydration and microstructures. *Constr. Build. Mater.* **2018**, *181*, 659–672. [CrossRef]
7. Sua-Iam, G.; Makul, N. Utilization of limestone powder to improve the properties of self-compacting concrete incorporating high volumes of untreated rice husk ash as fine aggregate. *Constr. Build. Mater.* **2013**, *38*, 455–464. [CrossRef]
8. Pokharel, M.; Fall, M. Combined influence of sulphate and temperature on the saturated hydraulic conductivity of hardened cemented paste backfill. *Cem. Concr. Compos.* **2013**, *38*, 21–28. [CrossRef]
9. Benzaazoua, M.; Ouellet, J.; Servant, S.; Newman, P.; Verburg, R. Cementitious backfill with high sulfur content: Physical, chemical and mineralogical characterization. *Cem. Concr. Res.* **1999**, *29*, 719–725. [CrossRef]
10. Hu, J.H.; Ren, Q.F.; Jiang, Q.; Gao, R.G.; Zhang, L.; Luo, Z.Q. Strength characteristics and the reaction mechanism of stone powder cement tailings backfill. *Adv. Mater. Sci. Eng.* **2018**, *2018*, 8651239. [CrossRef]
11. Fall, M.; Pokharel, M. Coupled effects of sulphate and temperature on the strength development of cemented tailings backfills: Portland cemen-paste backfill. *Cem. Concr. Compos.* **2010**, *32*, 819–828. [CrossRef]

12. Kesimal, A.; Yilmaz, E.; Ercikdi, B.; Alp, I.; Deveci, H. Effect of properties of tailings and binder on the short- and long-term strength and stability of cemented paste backfill. *Mater. Lett.* **2005**, *59*, 3703–3709. [CrossRef]
13. Zhou, K.P.; Gao, R.G.; Gao, F. Particle Flow Characteristics and Transportation Optimization of Superfine Unclassified Backfilling. *Miner* **2017**, *7*, 6. [CrossRef]
14. Ercikdi, B.; Kuekci, G.; Yilmaz, T. Utilization of granulated marble and waste bricks as mineral admixture in cemented paste backfill of sulphide-rich tailings. *Constr. Build. Mater.* **2015**, *93*, 573–583. [CrossRef]
15. Ye, G.; Liu, X.; de Schutter, G.; Poppe, A.M.; Taerwe, L. Influence of limestone powder used as filler in SCC on hydration and microstructure of cement pastes. *Cem. Concr. Res.* **2007**, *29*, 94–102. [CrossRef]
16. Hassani, F.P.; Ouellet, J.; Hossein, M. Strength development in underground high sulphate paste backfill operation. *CIM Bull.* **2001**, *1050*, 57–62.
17. Ouellet, S.; Bussiere, B.; Aubertin, M.; Benzaazoua, M. Characterization of cemented paste backfill pore structure using SE and IA analysis. *Bull. Eng. Geol. Environ.* **2008**, *67*, 139–152. [CrossRef]
18. Davy, C.A.; Adler, P.M. Three-scale analysis of the permeability of a natural shale. *Phys. Rev.* **2017**, *96*, 063116. [CrossRef] [PubMed]
19. Oh, B.H.; Jang, S.Y.; Shin, Y.S. Experimental investigation of the threshold chloride concentration for corrosion initiation in reinforced concrete structures. *Mag. Concr. Res.* **2001**, *55*, 441–504. [CrossRef]
20. Shang, J.L.; Hu, J.H.; Zhou, K.P.; Luo, X.W.; Aliyu, M. Porosity increment and strength degradation of low-porosity sedimentary rocks under different loading conditions. *Int. J. Rock Mech. Min. Sci.* **2015**, *75*, 216–223. [CrossRef]
21. Zhou, K.P.; Li, J.L.; Xu, Y.J.; Zhang, Y.M. Determination of pore structure characteristics of rock based on nuclear magnetic resonance. *J. Central South Univ. (Sci. Technol.)* **2012**, *43*, 4796–4800.
22. Wu, Z.W. High performance concrete-green concrete. *Chin. Concr. Cem. Prod.* **2000**, *2*, 1–4.
23. Zhou, S. Research on pore structure fractal characteristics of cement concrete. *Concrete* **2016**, *315*, 56–58.
24. Liu, G.Q.; Liu, S.X.; Huang, Q.J.; Zhong, Y.L.; Zhong, S.; Qin, X. Metallography and material microstructure quantitative analysis technology. *Chin. J. Stereol. Image Anal.* **2002**, *7*, 248–251.
25. Al-Kheetan, M.J.; Rahman, M.M.; Chamberlain, D.A. Development of hydrophobic concrete by adding dualcrystalline admixture at mixing stage. *Struct. Concr.* **2018**, *19*, 1504–1511. [CrossRef]